Topological thermal Hall effect and magnonic edge states in kagome ferromagnets with bond anisotropy

Fengjun Zhuo, Hang Li, Aurelien Manchon

Topological thermal Hall effect and magnonic edge states in kagome ferromagnets with bond anisotropy

Fengjun Zhuo (卓冯骏),[1,*] Hang Li,[2] and Aurélien Manchon[3,†]

[1]*King Abdullah University of Science and Technology (KAUST), Physical Science and Engineering Division (PSE), Thuwal 23955-6900, Saudi Arabia*
[2]*School of Physics and Electronics, Henan University, Kaifeng 475004, China*
[3]*Aix Marseille Univ, CNRS, CINAM, Marseille, France*

The magnon band topology due to the Dzyaloshinskii-Moriya interaction (DMI) and its relevant topological thermal Hall effect has been extensively studied in kagome lattice magnets. In this theoretical investigation, we report a new mechanism for phase transitions between topological phases of magnons in kagome ferromagnets by tuning the anisotropic nearest-neighbor ferromagnetic interaction and DMI. Using the linear spin-wave theory, we calculate the Chern number and thermal Hall conductivity of magnons in low temperature regime. We show the magnon band structures and magnonic edge states in each topological phase. From the topological phase diagram, we find a sign reversal of the thermal Hall conductivity upon tuning the modulation factors. We explicitly demonstrate the correspondence of thermal Hall conductivity with the propagation direction of the magnonic edge states. Finally, we discuss candidate materials as experimental realizations of our theoretical model.

I. INTRODUCTION

Magnonics, which aims to investigate the properties and control the transport of magnons in magnetic insulators, has attracted great interests in modern condensed matter physics [1–3]. Due to their nanometer wavelength and low energy consumption, magnons are considered as promising information carriers with great potential for data processing devices in the near future [4–6].

Concurrently, understanding the topological phases of matter in condensed matter physics has gained substantial momentum and several paradigms involving various (quasi)particle excitations have been investigated, including electrons [7–10], photons [11–13], phonons [14, 15], magnetic solitons [16–18] and magnons [19, 20]. Specifically in magnonic systems, the concept of topology has also been extended to topological magnon insulators (TMIs) [21–24], magnonic Dirac and Weyl semimetals [25–36], as well as magnonic nodal-line and triple-point semimetals [37–40]. Meanwhile, a growing number of theoretical and experimental studies has been devoted to investigating various topological features of magnon bands on specific lattice geometries, such as, pyrochlore [26, 41], honeycomb [25], Kitaev [42–44], triangular [45] and kagome lattice [46–51], as well as skyrmion crystals [52, 53]. However, in most of them, the nontrivial band topology is brought about by the Dzyaloshinskii-Moriya interaction (DMI) [54, 55], which plays a role analogous to the spin-orbit coupling in electronic systems lacking inversion symmetry [56–58].

Although a magnon is a charge-neutral quasiparticle immune to the Lorentz force usually experienced by charged particles, it experiences an effective magnetic field in momentum space induced by DMI [59, 60]. The magnon thermal Hall effect (THE) is characterized by a transverse thermal conductivity in response to a longitudinal temperature gradient, which has been realized experimentally in the pyrochlore ferromagnets [61, 62] and the kagome ferromagnets [46, 47]. The magnon THE was firstly explained as a result of noncompensated magnon edge currents by Matsumoto *et al.* [59]. Subsequently, studies have found that the net edge currents are closely related to the nontrivial magnonic edge states, and the sign of the thermal Hall conductivity is associated with the propagation direction of edge states [22, 63]. The unique nature of magnon THE has inspired lots of discoveries in phase transitions among magnonic topological phases. Heretofore the topological phase transitions for magnonic kagome lattices have been reported under a varying magnetic field [49, 50], magnon-phonon coupling [64–66] and next-nearest-neighbor (NNN) exchange interactions [67]. Recently, topological magnons in *XXZ* kagome lattice antiferromagnets have been widely investigated [32, 68, 69]. When generalized into a kagome lattice, three different nearest-neighbor (NN) hopping parameters could form an alternating pattern, giving rise to a rich variety of magnonic topological phases in two dimensions. From this point of view, it is tempting to ask whether a magnonic analog of the topological insulator exists and, more importantly, what non-trivial transverse transport properties of magnons are shown in such a system.

In this paper, we study a kagome ferromagnet with anisotropic NN ferromagnetic interaction and DMI as illustrated in Fig. 1. By varying the modulation factors η_1, η_2 and η_3, we find five different magnonic topological phases and plot the topological phase diagram in η_2-η_3 parameter plane. We moreover show the topological phase transition characterized by the Chern numbers of magnon bands, which can be detected by the change of magnon thermal Hall conductivity. We also demonstrate the correspondence between the thermal Hall conductivity and the propagation direction of the nontrivial edge states. Furthermore, we find sign changes of the thermal Hall conductivity coupled with the topological phase transition. The studies here will be useful for the future design of magnon-based devices, since the thermal Hall conductivity can be easily tuned via modulation factors.

* fengjun.zhuo@kaust.edu.sa
† manchon@cinam.univ-mrs.fr

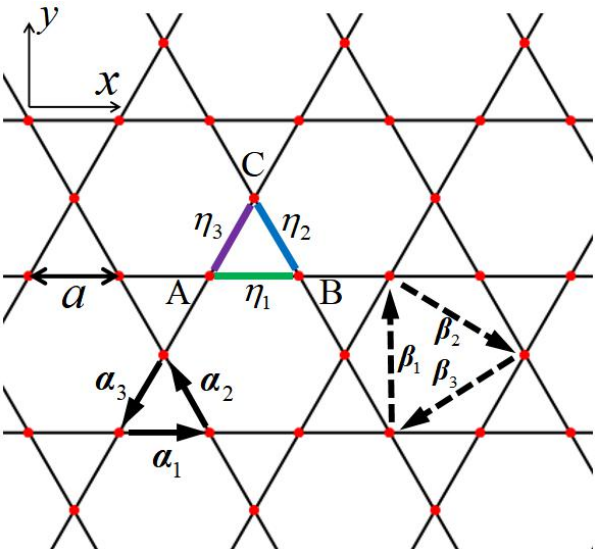

Figure 1. Schematics for the kagome ferromagnet with lattice constant a. Spin sublattices A, B, and C are placed at the corners of the triangles. η_1, η_2 and η_3 are the modulation factors along A-B bond (green line), B-C bond (blue line) and A-C bond (purple line) directions, respectively. The NN and second-NN connecting vectors are labeled by $\boldsymbol{\alpha}_i$ and $\boldsymbol{\beta}_i$.

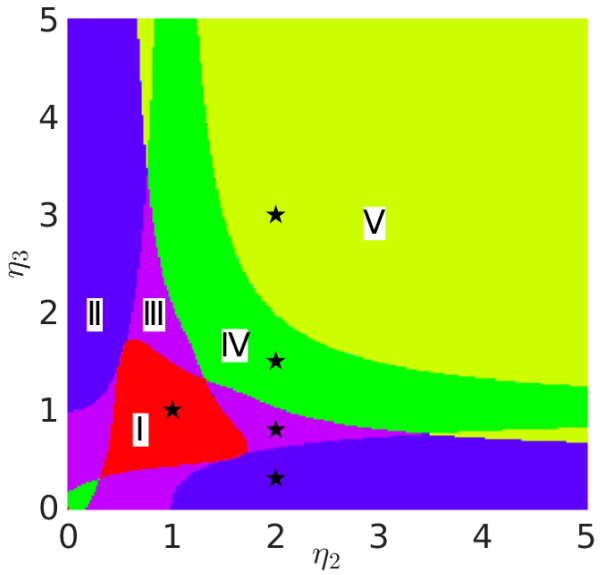

Figure 2. Topological phase diagram of the kagome lattice on the $\eta_2 - \eta_3$ plane with regions characterized by sets of Chern numbers. Five variable sets $\{\eta_2, \eta_3\}$ we use in later calculations are shown as black pentagrams in each topological phase.

The paper is organized as follows. In Sec. II we introduce our theoretical model and method. Detailed numerical results are presented in Sec. III, including the topological phase diagram, topological magnon band structures, magnonic edge modes, the thermal Hall conductivity. Finally, we end the paper with a brief discussion on the candidate materials and a summary in Sec. IV.

II. SPIN MODEL AND TOPOLOGICAL MAGNONS

Let us consider a collinear ferromagnet on a kagome lattice in the xy plane as schematically shown in Fig. 1. Its Hamiltonian reads

$$\begin{aligned}\mathcal{H} = &-\sum_{\langle ij\rangle} J_{ij}\boldsymbol{S}_i\cdot\boldsymbol{S}_j - J_2\sum_{\langle\langle ij\rangle\rangle}\boldsymbol{S}_i\cdot\boldsymbol{S}_j \\ &+\sum_{\langle ij\rangle} D_{ij}\epsilon_{ij}\hat{z}\cdot(\boldsymbol{S}_i\times\boldsymbol{S}_j)\,,\end{aligned} \tag{1}$$

where $\boldsymbol{S}_i$ is the vector of spin operators at site i. The first two terms describe the NN and NNN ferromagnetic interactions ($J_{ij}, J_2 > 0$), respectively. The third term is the out-of-plane NN DMI, where D_{ij} is the DMI strength and $\epsilon_{ij} = \pm 1$ depends on the chirality of the triangles in the kagome lattice. Specifically, the NN interactions J_{ij} and D_{ij} are modulated around its equilibrium value J_1 and D with different coefficients η_i depending on the bond direction as shown in Fig. 1: $J_{ij}\,(D_{ij}) = \eta_1 J_1\,(D)$ along $\boldsymbol{\alpha}_1$, $J_{ij}\,(D_{ij}) = \eta_2 J_1\,(D)$ along $\boldsymbol{\alpha}_2$ and $J_{ij}\,(D_{ij}) = \eta_3 J_1\,(D)$ along $\boldsymbol{\alpha}_3$ directions, respectively. The anisotropic NN interactions can be realized by lattice distortion induced by a controllable voltage or mechanical strain. Notice that such lattice deformations should change not only the NN exchange interactions but also the NNN ferromagnetic interactions. As discussed in the Appendix, the anisotropy of NNN ferromagnetic interactions does not produce new nontrivial band topology, introducing only restricted modifications to the band dispersion and distribution of Berry curvature. So for simplicity, we will treat the NNN ferromagnetic interactions as isotropic throughout this paper. In addition, the simultaneous changes of NN ferromagnetic interaction and DMI will preserve the collinear ferromagnetic ground state, because the DMI is well below the threshold value for a new spin configuration formation.

In the following, we apply a linear spin-wave theory to obtain the tight-binding magnon Hamiltonian in the momentum space. We express the spin operators in Eq. (1) in terms of magnon creation operator $\hat{b}_i^\dagger$ and annihilation operator $\hat{b}_i$ by using the Holstein-Primakoff transformations [70]: $S_i^+ = \sqrt{2S}b_i$, $S_i^+ = \sqrt{2S}b_i^\dagger$ and $S_i^z = S - b_i^\dagger b_i$, where we introduce the magnon ladder operators $S_i^\pm = S_i^x \pm iS_i^y$. We neglect the higher-order terms in the magnon operators from the magnon-magnon interactions, as we consider the low temperature regime here. After a Fourier transformation, Eq. (1) becomes $\mathcal{H} = S\sum_{\boldsymbol{k}}\Psi_{\boldsymbol{k}}^\dagger H(\boldsymbol{k})\Psi_{\boldsymbol{k}}$, where the tight-binding magnon Hamiltonian, $H = H_0 + H_{J_1} + H_D + H_{J_2}$, is a 3×3 matrix under the basis $\Psi_{\boldsymbol{k}}^\dagger = \left(b_A^\dagger, b_B^\dagger, b_C^\dagger\right)$. The submatrices of H read

$$H_0 = \begin{pmatrix} m_1 & 0 & 0 \\ 0 & m_2 & 0 \\ 0 & 0 & m_3 \end{pmatrix}, \tag{2a}$$

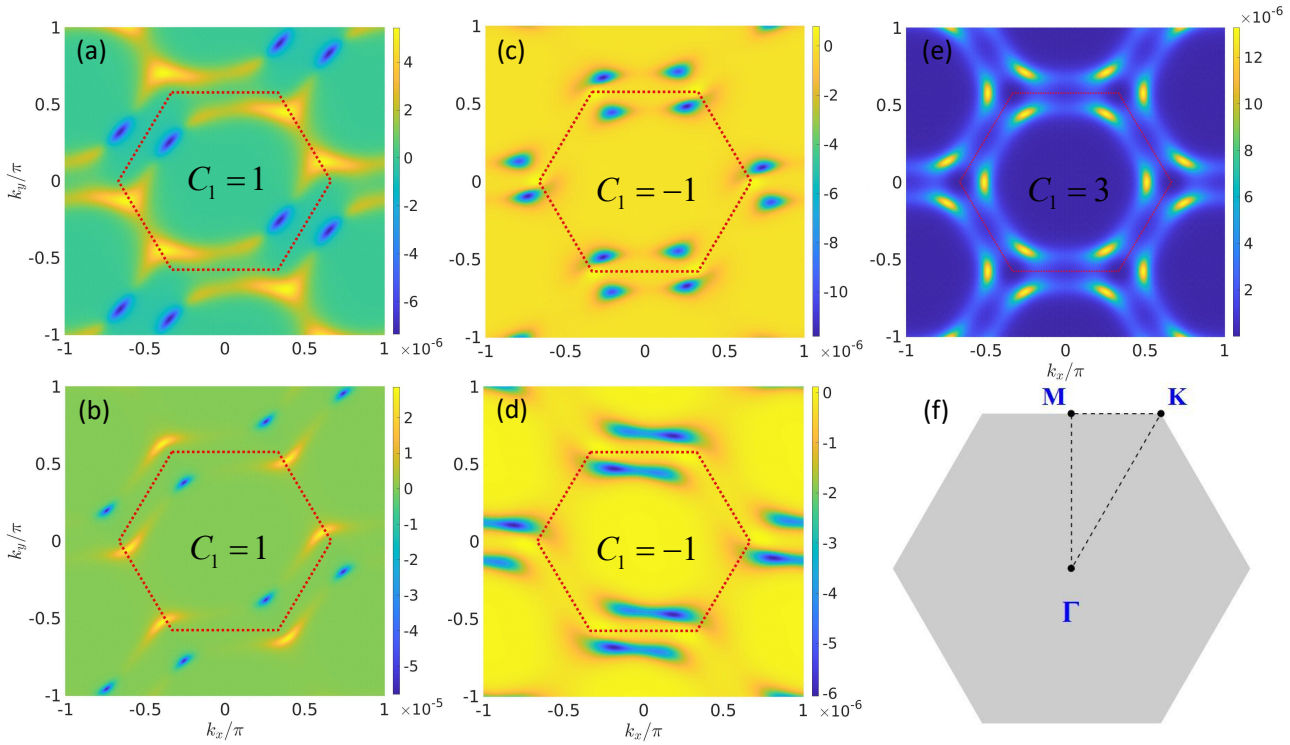

Figure 3. Berry curvatures of the lowest band with different modulation factors. (a) $\eta_2 = 2$ and $\eta_3 = 0.3$ in phase II. (b) $\eta_2 = 2$ and $\eta_3 = 0.8$ in phase III. (c) $\eta_2 = 2$ and $\eta_3 = 1.5$ in phase IV. (d) $\eta_2 = 2$ and $\eta_3 = 3$ in phase V. (e) $\eta_2 = 1$ and $\eta_3 = 1$ in phase I. Corresponding Chern numbers of the lowest band C_1 are given in each panel. The dotted red lines denote the edges of the first Brillouin zone. (f) The first Brillouin zone of the reciprocal lattice. The dotted black lines denote the selected k path connecting the high-symmetry points in the magnon bands shown in Fig. 4.

$$H_{J_1} = -2J_1 \begin{pmatrix} 0 & \gamma_1 & \gamma_3 \\ \gamma_1 & 0 & \gamma_2 \\ \gamma_3 & \gamma_2 & 0 \end{pmatrix}, \tag{2b}$$

$$H_D = -2iD \begin{pmatrix} 0 & \gamma_1 & -\gamma_3 \\ -\gamma_1 & 0 & \gamma_2 \\ \gamma_3 & -\gamma_2 & 0 \end{pmatrix}, \tag{2c}$$

$$H_{J_2} = -2J_2 \begin{pmatrix} 0 & \cos(\boldsymbol{k}\cdot\boldsymbol{\beta}_1) & \cos(\boldsymbol{k}\cdot\boldsymbol{\beta}_2) \\ \cos(\boldsymbol{k}\cdot\boldsymbol{\beta}_1) & 0 & \cos(\boldsymbol{k}\cdot\boldsymbol{\beta}_3) \\ \cos(\boldsymbol{k}\cdot\boldsymbol{\beta}_2) & \cos(\boldsymbol{k}\cdot\boldsymbol{\beta}_3) & 0 \end{pmatrix}, \tag{2d}$$

where $m_1 = 2J_1(\eta_1+\eta_3) + 4J_2$, $m_2 = 2J_1(\eta_1+\eta_2) + 4J_2$, $m_3 = 2J_1(\eta_2+\eta_3) + 4J_2$ and $\gamma_i = \eta_i \cos(\boldsymbol{k}\cdot\boldsymbol{\alpha}_i)$, respectively. The linking vectors $\boldsymbol{\alpha}_i$ and $\boldsymbol{\beta}_i$ are illustrated in Fig. 1.

In contrast to electronic systems, the absence of Fermi surface in bosonic systems leads to the ill-defined Chern number of magnons. However, the Chern number of magnons for the nth magnonic bulk band can still be given in a similar way,

$$C_n = \frac{1}{2\pi}\int_{BZ} dk^2 \Omega^z_{n\boldsymbol{k}}. \tag{3}$$

and the Berry curvature of magnons $\Omega^z_{n\boldsymbol{k}}$ is defined as

$$\Omega^z_{n\boldsymbol{k}} = -2\sum_{m\neq n} \mathrm{Im}\frac{\langle\psi_{n\boldsymbol{k}}|\partial_{k_x}H|\psi_{m\boldsymbol{k}}\rangle\langle\psi_{m\boldsymbol{k}}|\partial_{k_y}H|\psi_{n\boldsymbol{k}}\rangle}{(\varepsilon_{n\boldsymbol{k}}-\varepsilon_{m\boldsymbol{k}})^2}, \tag{4}$$

where $\psi_{n\boldsymbol{k}}$ and $\varepsilon_{n\boldsymbol{k}}$ are the eigenvectors and eigenvalues of $H(\boldsymbol{k})$ for the nth band, respectively. Another important quantity in topological systems is the winding number ν_m in band gap m, which is given by the sum of Chern numbers up to the mth band [71],

$$\nu_m = \sum_{n\leq m} C_n. \tag{5}$$

The winding number reflects the surface properties of the system, that is to say, we can find $|\nu_m|$ pairs of topologically nontrivial edge states in the mth band gap and their propagation direction is determined by the sign of ν_m.

The topological nature of magnonic edge states can be probed by measuring of the magnon thermal Hall effect in magnonic systems. The magnon thermal Hall conductivity is calculated using the following formula [59, 60]

$$\kappa_{xy} = -\frac{k_B^2 T}{\hbar}\sum_{n=1}^{3}\int_{BZ}\frac{d^2k}{(2\pi)^2}c_2\left[\rho^B(\varepsilon_{n\boldsymbol{k}})\right]\Omega^z_{n\boldsymbol{k}}, \tag{6}$$

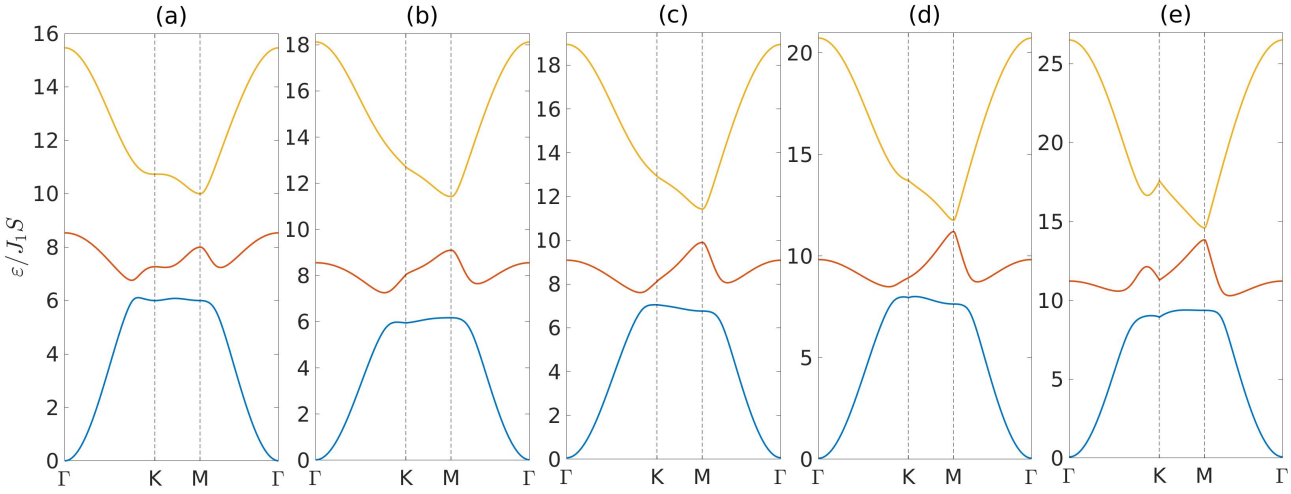

Figure 4. Magnon band structures of a kagome ferromagnet for the selected modulation factors in different topological phases. (a) $\eta_2 = 1$ and $\eta_3 = 1$ in phase I. (b) $\eta_2 = 2$ and $\eta_3 = 0.3$ in phase II. (c) $\eta_2 = 2$ and $\eta_3 = 0.8$ in phase III. (d) $\eta_2 = 2$ and $\eta_3 = 1.5$ in phase IV. (e) $\eta_2 = 2$ and $\eta_3 = 3$ in phase V.

where $\rho^B(\varepsilon_{n\boldsymbol{k}}) = \left(e^{\varepsilon_{n\boldsymbol{k}}/k_BT} - 1\right)^{-1}$ is the Bose-Einstein distribution. The weighting function is given by $c_2 = (1+x)\ln^2\frac{1+x}{x} - \ln^2 x - 2\mathrm{Li}_2(-x)$, with $\mathrm{Li}_2(x)$ being the polylogarithm function.

III. RESULTS

For the sake of simplicity, the Hamiltonian Eq. (1) is normalized to J_1S, so that energy, temperature and thermal conductivity are expressed in the units of J_1S, J_1S/k_B and $J_1S(k_B/\hbar)$, respectively. In the following numerical calculations, unless otherwise specified, $D = 1$ and $J_2 = 1$. Without loss of generality, we set $\eta_1 = 1$ as the scale unit, whereas η_2 and η_3 are tunable parameters. The Chern numbers of magnons are calculated by using the algorithm of Fukui et al. with 1000×1000 points in momentum space [72].

A. Topological phase diagram and band topology

As mentioned above, varying the anisotropic NN exchange interactions provides a handle to tune topological phase transitions in kagome ferromagnets. The topological phase diagram as a function of η_2 and η_3 is depicted in Fig. 2. These phases are characterized by sets of Chern numbers (C_1, C_2, C_3) of the lower, middle and upper magnon bulk bands, as shown in Fig. 4. Specifically, five different topological phases are found with Chern numbers: phase I $(3, -2, -1)$, phase II $(1, -1, 0)$, phase III $(1, 0, -1)$, phase IV $(-1, 2, -1)$ and phase V $(-1, 1, 0)$. In the following disscusion, we chose $\{\eta_2, \eta_3\} = \{1, 1\}$, $\{2, 0.3\}$, $\{2, 0.8\}$, $\{2, 1.5\}$ and $\{2, 3\}$ in each topological phase, all of which are marked by the black pentagrams in Fig. 2.

In Figs. 3(a)-3(e), we plot the distribution of Berry curvature $\Omega^z_{n\boldsymbol{k}}$ associated with the lower magnon band for five selected sets of modulation parameters $\{\eta_2, \eta_3\}$, that drive the system into five different topological phases. It is remarkable that the Berry curvature exhibits a $\mathbf{C}_2$ rotational symmetry in Figs. 3(a)-3(d) due to the anisotropic NN interactions, instead of a $\mathbf{C}_6$ rotational symmetry when $\eta_1 = \eta_2 = \eta_3$ shown in Fig. 3(e). The summation of $\Omega^z_{n\boldsymbol{k}}$ over the first Brillouin zone gives the corresponding Chern number of the lower band C_1. Then, we turn our attention to the exploration of the band topology in kagome ferromagnets. Fig. 4 shows the magnon bulk bands along the high-symmetry directions $(\Gamma - K - M - \Gamma)$ of the Brillouin zone [Fig. 3(f)] in each topological phase. Three well separated magnon bands, *i.e.*, two well defined band gaps, can be found in all phases. The upper band is close to the middle band at M point with increasing η_3 when $\eta_2 = 2$ as shown in Figs. 4(b)-4(e). We also note that the Berry curvature exhibits higher densities when the band gap is shifted towards closing, for example, the peaks of Berry curvature along $\Gamma - K$ line and near K point in Figs. 3(c) and 3(e).

To better visualize the magnonic edge states, we solve the eigenvalue problem of a nanoribbon geometry with open boundary conditions, and then plot the band structures in Fig. 5. The winding numbers in phase II are $\nu_1 = 1$ and $\nu_2 = 0$, so two crossed chiral edge states are clearly found in the lower band gap and two gapped trivial edge states are found in the upper band gap, as shown in Fig. 5(a). In phase III, as the two winding numbers are the same, $\nu_1 = \nu_2 = 1$, two equivalent pairs of nontrivial edge states emerge in each band gap in Fig. 5(b). As η_3 is further increasing, the nonzero winding numbers in phase IV are $\nu_1 = -1$ and $\nu_2 = 1$, and we can find two pairs of nontrivial edge states in the two band gaps in Fig. 5(c). Meanwhile, the edge states have opposite slopes $v_g = \partial\varepsilon/\partial k$ (*i.e.*, group velocity): the red one moves from the bottom left to the top right ($v_g > 0$) in the lower gap; instead, the red one moves from the top left to the bottom right ($v_g < 0$) in the upper gap. In other words, they propa-

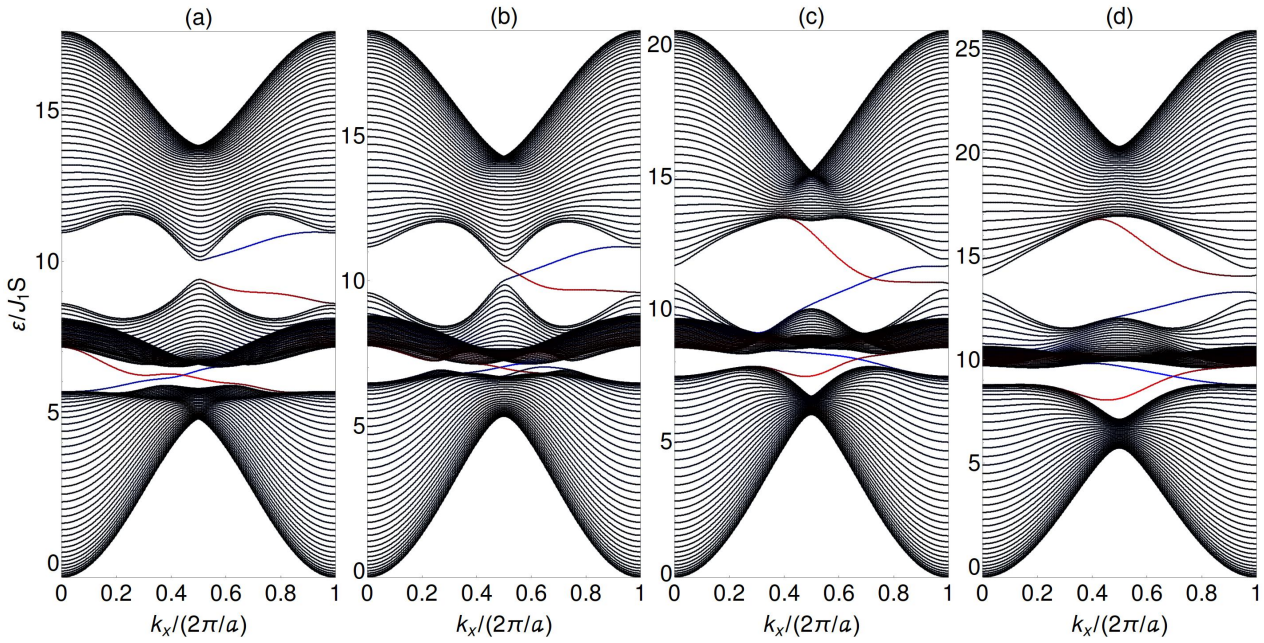

Figure 5. Magnon band structure with coupled magnonic edge states in a kagome ferromagnet with a nanoribbon geometry at different modulation factors. (a) $\eta_2 = 2$ and $\eta_3 = 0.3$ in phase II. (b) $\eta_2 = 2$ and $\eta_3 = 0.8$ in phase III. (c) $\eta_2 = 2$ and $\eta_3 = 1.5$ in phase IV. (d) $\eta_2 = 2$ and $\eta_3 = 3$ in phase V. The black lines are the magnon bulk bands. The blue/red lines represent the edge states for the upper/lower edges.

gate in opposite directions. Finally, the system has a pair of nontrivial edge states in the lower gap and a pair of trivial edge states in the upper gap with $\nu_1 = -1$ and $\nu_2 = 0$, as shown in Fig. 5(d). Note that the propagation directions of the nontrivial edge states in the lower gap are opposite in Figs. 5(a)-5(b) and Figs. 5(c)-5(d).

B. Topological thermal Hall effect

In this section, we discuss the topological nature of magnon THE. In magnonic systems, the topological phases and phase transitions can be detected by the measurement of magnon dispersion using inelastic neutron scattering [47]. In Fig. 6, the magnon thermal Hall conductivity κ_{xy} in low temperature regime is plotted as a function of temperature with different modulation factors $\{\eta_2, \eta_3\}$ in each topological phases, which all show a monotonically increasing behavior. We also find $\kappa_{xy} < 0$ in phase I, II and III, conversely, $\kappa_{xy} > 0$ in phase IV and phase V.

The thermal Hall conductivity κ_{xy} as a function of η_3 when $\eta_2 = 2$ for four different temperatures are depicted in Fig. 7. The system undergoes the phase transition from phase II to phase V, as η_3 increases from 0 to 3. In addition, we find a sign reversal of κ_{xy} when the topological phase transits between phases III and IV, which can be explained by connecting the propagation directions of the nontrivial edge states. From Eq. (4) and Eq. (6), we see that C_n and κ_{xy} only have different

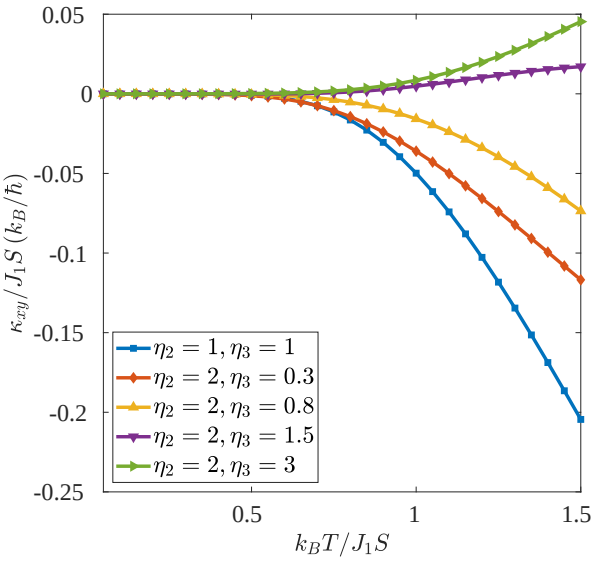

Figure 6. The magnon thermal Hall conductivity in low temperature regime as a function of temperature for different modulation factors $\{\eta_2, \eta_3\}$ in each topological phase.

weighting functions in the integrand. Hence, the dominant contribution to the thermal Hall conductivity at low temperatures comes from the lowest band, since the lowest band is more occupied due to the c_2 function within the bosonic statis-

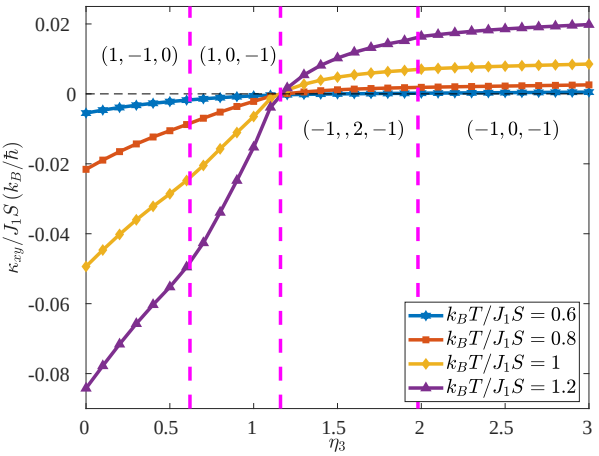

Figure 7. Topological thermal Hall conductivity in low temperature regime versus modulation factor η_3 at different temperatures with $\eta_2 = 2$. Four different topological phases labeled with Chern numbers are separated by the critical points shown as vertical dashed magenta lines.

tics. As a consequence, the sign of κ_{xy} is governed by the sign of ν_1 in low temperature regime as $\nu_1 = C_1$. As we mentioned above, the propagation directions of edge states in the lower gap are opposite between the topological phases III and IV. Finally, the sign reversal of κ_{xy} is accompanied by the sign reversal of ν_1, even though the two pairs of nontrivial edge states also have opposite propagation directions in phase IV.

IV. DISCUSSION AND SUMMARY

In this paper, a tunable topological magnon excitation in kagome lattice ferromagnets has been predicted. We shall further briefly comment on the candidate materials for experimental realizations of the above theoretical model. Recent experiments show that the materials Cu(1-3,bdc) [46, 47], as well as the mineral haydeeite—α-$MgCu_3(OD)_6Cl_2$ [48], exhibit a stable ferromagnetic phase down to the monolayer limit. In these materials, magnetic ions are arranged on a kagome lattice with their magnetization pointing perpendicular to the plane. Meanwhile, the variations of the NN interactions can be easily achieved from the lattice distortions induced by applying external perturbations, such as mechanical strain or pressure, because the interactions depend sensitively on the inter-atomic distances [73–76]. The different types of strains studied in the present work can be achieved and tuned by applying a uniaxial mechanical strain field, either along different crystallographic directions. For instance, a uniaxial strain along $\boldsymbol{\alpha}_1$ direction shall result in $\eta_2 = \eta_3 \neq \eta_1$. Using the parameters in Ref. [48], we can find a thermal Hall conductivity of -3.2×10^{-3} W/Km with isotropic NN interaction ($\eta_2 = \eta_3 = \eta_1$) and 3.2×10^{-3} W/Km with anisotropic NN interaction ($\eta_2 = \eta_3 = 2\eta_1$) at the temperature $T = 50$ K. Tuning the anisotropy parameters over a wide range to cover the diagram reported on Fig. 2 remains a technical challenge that can be achieved by depositing the kagome ferromagnet on a piezoelectric substrate for instance [77, 78]. Detailed first-principles calculations are needed to identify suitable interfaces [79].

Thus far, we have studied the magnon Hall effect in a picture of magnons within the bosonic description. As mentioned in Sec. II, we truncate the bosonic Hamiltonian to quadratic order by neglecting the magnon-magnon interaction in the low temperature regime. However, by using the Holstein-Primakoff transformations, it is unclear whether the quartic terms for the interaction between magnons could be ignored. In this perspective, another theoretical formalism of the thermal Hall effect was developed in the language of spin operators instead of boson operators [80]. In this formalism, the thermal Hall effect in a correlated paramagnetic phase can also be captured with reductions to the Schwinger-boson representation of spin operators by using self-consistent mean-field theory. Remarkably, the thermal Hall coefficients obtained from the linear-response theory for noninteracting models [59] and the mean-field Hamiltonian for the interacting spin model are identical. On the other hand, as low-energy charge-neutral excitations, phonons can also carry angular momenta [81–83] and induce a transverse phonon angular momentum flows at finite temperatures, the so-called phonon thermal Hall effect [14]. However, the phonon angular momenta in a phonon Hall current can only create negligible accumulation at the crystal edges in comparison with the magnon spin moment accumulation in a magnon Hall current [84, 85]. In addition, since the magnon-phonon interaction may significantly modify the magnon-mediated THE due to symmetry breaking by an in-plane DMI and the magnetoelastic coupling [64, 86, 87], its role on the nontrivial topology of magnon excitation would be an interesting topic left to future studies [87]. Since magnon-magnon interactions and magnon-phonon interactions need to be taken into consideration at high temperatures, the linear spin-wave theory becomes inaccurate in this limit. However, self-consistent Holstein-Primakoff and Schwinger-boson methods within Hartree-Fock mean-field approximation will be applicable to computation of the thermal Hall response functions [80, 88], which goes beyond the scope of this paper.

In summary, we have shown that tuning the relative strength of anisotropic NN ferromagnetic interaction and DMI in kagome ferromagnets gives rise to the topological phase transition between different topological phases characterized by the Chern numbers of magnon bands. We describe the band topology of magnons with the magnonic edge states in the band gaps. Furthermore, we have calculated the thermal Hall conductivity κ_{xy} and expound its relevance to the topological invariant ν_m. We find that κ_{xy} can easily be controlled by tuning the modulation factors. In addition, a sign reversal of κ_{xy} was found along with topological phase transitions. In this regard, the present studies open thrilling perspectives for experimentalists and can be applied in the field of thermal micro-sensors in the future.

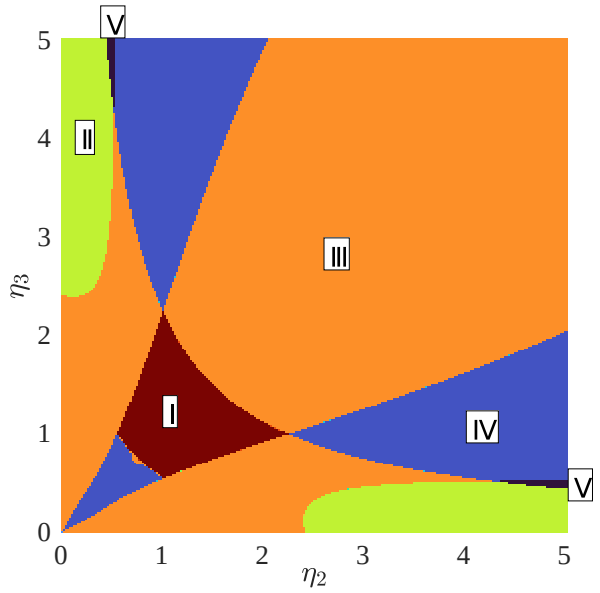

Figure 8. Topological phase diagram on the $\eta_2 - \eta_3$ plane with regions characterized by sets of Chern numbers when taking anisotropic next-nearest-neighbor exchange interactions into consideration. Five different topological phases are labeled with the same Chern numbers as shown in Fig. 2.

ACKNOWLEDGEMENTS

F.Z. was supported by King Abdullah University of Science and Technology (KAUST). A.M. acknowledges support from the Excellence Initiative of Aix-Marseille Université—A*Midex, a French "Investissements d'Avenir" program. H.L. acknowledge the support from Henan University (No. CJ3050A0240050) and National Natural Science Foundation of China (No. 11804078).

APPENDIX: ANISOTROPIC NEXT-NEAREST-NEIGHBOR EXCHANGE INTERACTIONS

As described in the main text, we propose that the topological phase transition can be tuned in kagome ferromagnets with anisotropic NN interactions. Generally speaking, such NN bond anisotropy may also influence the NNN ferromagnetic interactions. In this case, the new Hamiltonian reads

$$\begin{aligned}\mathcal{H} = &-\sum_{\langle ij\rangle} J_{ij}\boldsymbol{S}_i\cdot\boldsymbol{S}_j - \sum_{\langle\langle ij\rangle\rangle} J'_{ij}\boldsymbol{S}_i\cdot\boldsymbol{S}_j \\ &+\sum_{\langle ij\rangle} D_{ij}\epsilon_{ij}\hat{z}\cdot(\boldsymbol{S}_i\times\boldsymbol{S}_j)\,,\end{aligned} \tag{A.1}$$

where the anisotropic NNN ferromagnetic interactions J'_{ij} are given as $J'_1 = \eta_2\eta_3 J_2$ along $\boldsymbol{\beta}_1$, $J'_2 = \eta_1\eta_2 J_2$ along $\boldsymbol{\beta}_2$, and $J'_3 = \eta_1\eta_3 J_2$ along $\boldsymbol{\beta}_3$, respectively. The corresponding submatrix H_{J_2} becomes

$$H_{J_2} = -2\begin{pmatrix} 0 & \mu_1 & \mu_2 \\ \mu_1 & 0 & \mu_3 \\ \mu_2 & \mu_3 & 0 \end{pmatrix} \tag{A.2}$$

with $\mu_i = J'_i\cos(\boldsymbol{k}\cdot\boldsymbol{\beta}_i)$. Here, all other parameters have the same meanings and values as mentioned in the main text.

Fig. 8 shows the topological phase diagram as a function of η_2 and η_3 when taking anisotropic NNN ferromagnetic interactions into consideration. In comparison with the topological phase diagram in Fig. 2, both phase diagrams are divided into five identical phases listed in the main text. In other words, there's no other nontrivial topological phase creating. In addition to that, the anisotropic NNN ferromagnetic interactions redistribute the region of each phase, as the specific magnon band dispersions and distributions of Berry curvature are modified by the difference between the NNN ferromagnetic interactions.

[1] V. Kruglyak, S. Demokritov, and D. Grundler, J. Phys. D: Appl. Phys. **43**, 264001 (2010).
[2] A. Serga, A. Chumak, and B. Hillebrands, J. Phys. D: Appl. Phys. **43**, 264002 (2010).
[3] S.-K. Kim, J. Phys. D: Appl. Phys. **43**, 264004 (2010).
[4] A. Khitun, M. Bao, and K. L. Wang, J. Phys. D: Appl. Phys. **43**, 264005 (2010).
[5] B. Lenk, H. Ulrichs, F. Garbs, and M. Münzenberg, Phys. Rep. **507**, 107 (2011).
[6] A. V. Chumak, V. I. Vasyuchka, A. A. Serga, and B. Hillebrands, Nat. Phys. **11**, 453 (2015).
[7] M. Z. Hasan and C. L. Kane, Rev. Mod. Phys. **82**, 3045 (2010).
[8] X.-L. Qi and S.-C. Zhang, Rev. Mod. Phys. **83**, 1057 (2011).
[9] M. Z. Hasan and J. E. Moore, Annu. Rev. Condens. Matter Phys. **2**, 55 (2011).
[10] B. Yan and S.-C. Zhang, Rep. Prog. Phys. **75**, 096501 (2012).
[11] L. Lu, J. D. Joannopoulos, and M. Soljačić, Nat. Photon. **8**, 821 (2014).
[12] A. B. Khanikaev and G. Shvets, Nat. Photon. **11**, 763 (2017).
[13] T. Ozawa, H. M. Price, A. Amo, N. Goldman, M. Hafezi, L. Lu, M. C. Rechtsman, D. Schuster, J. Simon, O. Zilberberg, *et al.*, Rev. Mod. Phys. **91**, 015006 (2019).
[14] L. Zhang, J. Ren, J.-S. Wang, and B. Li, Phys. Rev. Lett. **105**, 225901 (2010).
[15] R. Süsstrunk and S. D. Huber, Science **349**, 47 (2015).
[16] B. Göbel, A. Mook, J. Henk, and I. Mertig, Phys. Rev. B **95**, 094413 (2017).
[17] B. Göbel, I. Mertig, and O. A. Tretiakov, Phys. Rep. **895**, 1 (2021).
[18] Z.-X. Li, Y. Cao, and P. Yan, Phys. Rep. **915**, 1 (2021).
[19] H. Katsura, N. Nagaosa, and P. A. Lee, Phys. Rev. Lett. **104**, 066403 (2010).
[20] V. Bonbien, F. Zhuo, A. Salimath, O. Ly, A. Abbout, and A. Manchon, J. Phys. D: Appl. Phys. **55** 103002 (2021).
[21] R. Shindou, R. Matsumoto, S. Murakami, and J.-i. Ohe, Phys. Rev. B **87**, 174427 (2013).
[22] L. Zhang, J. Ren, J.-S. Wang, and B. Li, Phys. Rev. B **87**, 144101 (2013).

[23] K. Nakata, S. K. Kim, J. Klinovaja, and D. Loss, Phys. Rev. B **96**, 224414 (2017).
[24] A. Rückriegel, A. Brataas, and R. A. Duine, Phys. Rev. B **97**, 081106 (2018).
[25] S. S. Pershoguba, S. Banerjee, J. C. Lashley, J. Park, H. Ågren, G. Aeppli, and A. V. Balatsky, Phys. Rev. X **8**, 011010 (2018).
[26] F.-Y. Li, Y.-D. Li, Y. B. Kim, L. Balents, Y. Yu, and G. Chen, Nat. commun. **7**, 1 (2016).
[27] J. Fransson, A. M. Black-Schaffer, and A. V. Balatsky, Phys. Rev. B **94**, 075401 (2016).
[28] N. Okuma, Phys. Rev. Lett. **119**, 107205 (2017).
[29] K. Li, C. Li, J. Hu, Y. Li, and C. Fang, Phys. Rev. Lett. **119**, 247202 (2017).
[30] V. A. Zyuzin and A. A. Kovalev, Phys. Rev. B **97**, 174407 (2018).
[31] B. Li and A. A. Kovalev, Phys. Rev. B **97**, 174413 (2018).
[32] S. A. Owerre, Phys. Rev. B **95**, 014422 (2017).
[33] S. A. Owerre, Phys. Rev. B **97**, 094412 (2018).
[34] S.-K. Jian and W. Nie, Phys. Rev. B **97**, 115162 (2018).
[35] Y. Su, X. S. Wang, and X. R. Wang, Phys. Rev. B **95**, 224403 (2017).
[36] Y. Su and X. R. Wang, Phys. Rev. B **96**, 104437 (2017).
[37] K. Hwang, N. Trivedi, and M. Randeria, Phys. Rev. Lett. **125**, 047203 (2020).
[38] S. Owerre, Sci. Rep. **7**, 1 (2017).
[39] S. Owerre, J. Phys.: Condens. Matter **30**, 28LT01 (2018).
[40] S. Owerre, Europhys. Lett. **125**, 36002 (2019).
[41] A. Mook, J. Henk, and I. Mertig, Phys. Rev. Lett. **117**, 157204 (2016).
[42] P. A. McClarty, X.-Y. Dong, M. Gohlke, J. G. Rau, F. Pollmann, R. Moessner, and K. Penc, Phys. Rev. B **98**, 060404 (2018).
[43] D. G. Joshi, Phys. Rev. B **98**, 060405 (2018).
[44] E. Aguilera, R. Jaeschke-Ubiergo, N. Vidal-Silva, L. E. F. F. Torres, and A. S. Nunez, Phys. Rev. B **102**, 024409 (2020).
[45] K.-S. Kim, K. H. Lee, S. B. Chung, and J.-G. Park, Phys. Rev. B **100**, 064412 (2019).
[46] M. Hirschberger, R. Chisnell, Y. S. Lee, and N. P. Ong, Phys. Rev. Lett. **115**, 106603 (2015).
[47] R. Chisnell, J. S. Helton, D. E. Freedman, D. K. Singh, R. I. Bewley, D. G. Nocera, and Y. S. Lee, Phys. Rev. Lett. **115**, 147201 (2015).
[48] D. Boldrin, B. Fåk, M. Enderle, S. Bieri, J. Ollivier, S. Rols, P. Manuel, and A. S. Wills, Phys. Rev. B **91**, 220408 (2015).
[49] P. Laurell and G. A. Fiete, Phys. Rev. B **98**, 094419 (2018).
[50] Y. Lu, X. Guo, V. Koval, and C. Jia, Phys. Rev. B **99**, 054409 (2019).
[51] A. Mook, J. Henk, and I. Mertig, Phys. Rev. B **99**, 014427 (2019).
[52] S. A. Díaz, J. Klinovaja, and D. Loss, Phys. Rev. Lett. **122**, 187203 (2019).
[53] S. A. Díaz, T. Hirosawa, J. Klinovaja, and D. Loss, Phys. Rev. Research **2**, 013231 (2020).
[54] I. Dzyaloshinsky, J. Phys. Chem. Sol. **4**, 241 (1958).
[55] T. Moriya, Phys. Rev. **120**, 91 (1960).
[56] A. Manchon, H. C. Koo, J. Nitta, S. Frolov, and R. Duine, Nat. Mater. **14**, 871 (2015).
[57] A. Belabbes, G. Bihlmayer, F. Bechstedt, S. Blügel, and A. Manchon, Phys. Rev. Lett. **117**, 247202 (2016).
[58] A. Manchon, J. Železný, I. M. Miron, T. Jungwirth, J. Sinova, A. Thiaville, K. Garello, and P. Gambardella, Rev. Mod. Phys. **91**, 035004 (2019).
[59] R. Matsumoto and S. Murakami, Phys. Rev. Lett. **106**, 197202 (2011).
[60] R. Matsumoto, R. Shindou, and S. Murakami, Phys. Rev. B **89**, 054420 (2014).
[61] Y. Onose, T. Ideue, H. Katsura, Y. Shiomi, N. Nagaosa, and Y. Tokura, Science **329**, 297 (2010).
[62] T. Ideue, Y. Onose, H. Katsura, Y. Shiomi, S. Ishiwata, N. Nagaosa, and Y. Tokura, Phys. Rev. B **85**, 134411 (2012).
[63] A. Mook, J. Henk, and I. Mertig, Phys. Rev. B **90**, 024412 (2014).
[64] X. Zhang, Y. Zhang, S. Okamoto, and D. Xiao, Phys. Rev. Lett. **123**, 167202 (2019).
[65] E. Thingstad, A. Kamra, A. Brataas, and A. Sudbø, Phys. Rev. Lett. **122**, 107201 (2019).
[66] S. Zhang, G. Go, K.-J. Lee, and S. K. Kim, Phys. Rev. Lett. **124**, 147204 (2020).
[67] A. Mook, J. Henk, and I. Mertig, Phys. Rev. B **89**, 134409 (2014).
[68] R. Seshadri and D. Sen, Phys. Rev. B **97**, 134411 (2018).
[69] F. A. Gómez Albarracín, H. D. Rosales, and P. Pujol, Phys. Rev. B **103**, 054405 (2021).
[70] T. Holstein and H. Primakoff, Phys. Rev. **58**, 1098 (1940).
[71] Y. Hatsugai, Phys. Rev. Lett. **71**, 3697 (1993).
[72] T. Fukui, Y. Hatsugai, and H. Suzuki, J. Phys. Soc. Jpn. **74**, 1674 (2005).
[73] F. Guinea, M. Katsnelson, and A. Geim, Nat. Phys. **6**, 30 (2010).
[74] M. Bahramy, B.-J. Yang, R. Arita, and N. Nagaosa, Nat. Commun. **3**, 1 (2012).
[75] L. Webster and J.-A. Yan, Phys. Rev. B **98**, 144411 (2018).
[76] T. Mukherjee, S. Chowdhury, D. Jana, and L. L. Y. Voon, J. Phys.: Condens. Matter **31**, 335802 (2019).
[77] C. Thiele, K. Dörr, O. Bilani, J. Rödel, and L. Schultz, Phys. Rev. B **75**, 054408 (2007).
[78] A. Herklotz, A. D. Rata, L. Schultz, and K. Dörr, Phys. Rev. B **79**, 092409 (2009).
[79] F. Zhuo, H. Li, and A. Manchon, Phys. Rev. B **104**, 144422 (2021).
[80] H. Lee, J. H. Han, and P. A. Lee, Phys. Rev. B **91**, 125413 (2015).
[81] L. Zhang and Q. Niu, Phys. Rev. Lett. **112**, 085503 (2014).
[82] M. Hamada, E. Minamitani, M. Hirayama, and S. Murakami, Phys. Rev. Lett. **121**, 175301 (2018).
[83] D. A. Garanin and E. M. Chudnovsky, Phys. Rev. B **92**, 024421 (2015).
[84] D. M. Juraschek and N. A. Spaldin, Phys. Rev. Materials **3**, 064405 (2019).
[85] S. Park and B.-J. Yang, Nano Lett. **20**, 7694 (2020).
[86] R. Takahashi and N. Nagaosa, Phys. Rev. Lett. **117**, 217205 (2016).
[87] G. Go, S. K. Kim, and K.-J. Lee, Phys. Rev. Lett. **123**, 237207 (2019).
[88] M. Shiranzaei, R. E. Troncoso, J. Fransson, A. Brataas, and A. Qaiumzadeh, arXiv:2108.08374 (2021).